Sensors & Actuators: B. Chemical 297 (2019) 126732

Contents lists available at ScienceDirect

Sensors and Actuators B: Chemical

journal homepage: www.elsevier.com/locate/snb

Design of a mid-infrared suspended chalcogenide/silica-on-silicon slot-waveguide spectroscopic gas sensor with enhanced light-gas interaction effect

Mingquan Pi[a], Chuantao Zheng[a,*], Ran Bi[a], Huan Zhao[a], Lei Liang[b], Yu Zhang[a], Yiding Wang[a], Frank K. Tittel[c]

[a] State Key Laboratory of Integrated Optoelectronics, College of Electronic Science and Engineering, Jilin University, 2699 Qianjin Street, Changchun, 130012, China
[b] State Key Laboratory of Luminescence and Applications, Changchun Institute of Optics Fine Mechanics and Physics, Chinese Academy of Sciences, Changchun 130033, China
[c] Department of Electrical and Computer Engineering, Rice University, 6100 Main Street, Houston, TX 77005, USA

ARTICLE INFO

Keywords:
Waveguide sensor
Suspended chalcogenide/silica-on-silicon slot-waveguide
Gas sensor
Mid-infrared absorption spectroscopy

ABSTRACT

The reported chalcogenide (ChG) waveguide sensor mainly focuses on rectangular waveguide with a small evanescent field for light-gas interaction. In order to improve the sensing performance in the mid-infrared spectral range and ease wavguide fabrication, a suspended ChG/silica-on-silicon slot-waveguide gas sensor was proposed, where ChG was used as the core layer, silica was adopted as the lower buffer as well as a support layer with the silica under the waveguide core removed. The new sensor structure resulted in an increased light-gas interaction, a decreased waveguide loss in the mid-infrared and a small depth-to-width ratio for feasible slot fabrication. The optimized suspended slot waveguide reveals a large power confinement factor (PCF) of 85.77% at 3291 nm. CH_4 was adopted as the target gas for performance evaluation of the ChG/silica-on-silicon slot-waveguide sensor at the absorption line of 3038.5 cm^{-1}. An optimal waveguide length of 1.45 cm was determined with a waveguide loss of 3 dB/cm for maximizing the sensitivity. The response time is as short as < 3 μs due to the exposure of the waveguide sensing area to the atmosphere. The limit of detection (LoD) was decided to be 1.70 parts-per-million (ppm) for a minimum detectable signal-to-noise ratio of 10. Effects of ambient temperature/pressure change and fabrication error on the sensor performance were discussed. The proposed suspended ChG/silica-on-silicon slot-waveguide sensor possesses a ~ 10 times larger PCF than other reported ChG rectangular waveguide sensors in the mid-infrared and reveals an improved performance for potential environmental monitoring and wearable gas sensing applications.

1. Introduction

Most gas species have a strong fundamental absorption in the mid-infrared (mid-IR) spectral range (2.5–20 μm), which is suitable for trace-level gas detection and quantification. Mid-IR gas sensor systems based on discrete devices (e.g. various optics, multipass gas cell, cavity) are widely reported [1–5]. However, these systems are large in size and power consumption and are sensitive to vibration and environmental changes. Compared to a large-sized sensor system, an on-chip waveguide sensor is more preferable in terms of the above properties, which has been increasingly used in various fields, such as chemical detection [6], clinical diagnosis [7], gas measurements [8], bio-sensing and environmental sensing [9,10]. A waveguide sensor can be fabricated on a single chip with ultra-compact size, capable of portable or even wearable detection [11]. Also, such a sensor, with the ability of real-time and in-situ detection [12], is a label-free sensor [13], causing no influence to the analyte. With a mature fabrication and integration technology, the cost of a waveguide sensor can be decreased providing the possibility of numerous applications.

There are two primary considerations during the design of an on-chip waveguide gas sensor based on mid-IR absorption. One consideration is the waveguide material to obtain low loss in the mid-IR band. Although silicon (Si) has a low propagation loss as the wavelength is < 8.5 μm [14], SOI platform is unsuitable in the mid-IR range because silica (SiO_2) is transparent below 3.6 μm. However, sulfide (S), selenide (Se) and Telluride (Te) have a wide transmittance in the mid-IR range up to 12 μm, 15 μm and 20 μm, respectively [15]. Therefore, chalcogenide (ChG) glasses, with the basic ingredient of S, Se and Te

* Corresponding author.
E-mail address: zhengchuantao@jlu.edu.cn (C. Zheng).

https://doi.org/10.1016/j.snb.2019.126732
Received 12 April 2019; Received in revised form 7 June 2019; Accepted 24 June 2019
Available online 25 June 2019
0925-4005/

mixing with arsenic (As), gallium (Ga) and germanium (Ge), are best qualified as waveguide core and buffer materials for gas sensing in the mid-IR range.

The other consideration is waveguide structure. The power confinement factor (PCF) of the reported ChG rectangular waveguide, which indicates the strength of light-gas interaction, is generally small due to the weak evanescent field. For example, J. Charrier et al. proposed a Ge-Sb-Se rectangular waveguide with a PCF of 5.8% [16]; A. Gutierrez-Arroyo et al. demonstrated two kinds of Ge-Sb-Se rectangular waveguides with a PCF of 8% and 5%, respectively [15,17]. In order to decrease the limit of detection (LoD) and reduce the device size, spiral and flexural rectangular waveguide structures with large waveguide length have been proposed [15,18]. For example, Z. Han et al. [19] proposed a $Ge_{23}Sb_7S_{70}$ rectangular waveguide with spiral shape for gas sensing, which possessed a waveguide length of 2 cm. Since a large PCF means not only low LoD, but also high sensitivity, the key factor for improving sensing performance is increasing PCF. By adopting the target gas as low-index material in the slot area, a slot-waveguide offers high light confinement in the slot area, leading to an enhanced light-gas interaction. For example, B. Kumari et al. proposed a parallel double-slot silicon rib waveguide with a high PCF of up to 68% [11]. However, slot-waveguide using ChG as core and buffer layer material hasn't been reported, due to a high depth-to-width ratio for single-mode propagation resulting in a large difficulty in fabrication.

In order to obtain an enhanced light-gas interaction effect as well as easy fabrication process in the mid-infrared, a novel suspended ChG/silica-on-silicon slot-waveguide structure was reported with a high PCF of more than 80%. The novel aspects of this sensor structure include: (1) Slot-waveguide structure is proposed to enhance the light-gas interaction by filling the target gas into the slot area; (2) ChG is adopted as the core material for enabling low waveguide loss in the mid-infrared for gas detection; (3) Silica instead of ChG material is used as a lower support buffer layer, and the silica under the waveguide core is removed, leading to a further increased light-gas interaction effect and a decreased waveguide loss by making the silica layer to be far away from the core. (4) Due to a large refractive index difference between the ChG material and air (target gas), the suspended ChG/silica-on-silicon slot-waveguide has an acceptable depth-to-width ratio, which makes the fabrication of the waveguide sensor easier. The waveguide parameters, including slot width, strip width, slot height and the dimensions of the suspended area were optimized for guided mode propagation, PCF enhancement and reasonable fabrication. Methane (CH_4) was adopted as the target gas for performance evaluation of the waveguide sensor at the absorption line of 3038.5 cm^{-1}, involving sensitivity, optimal waveguide length and LoD. Tolerances of fabrication error, temperature and pressure change were discussed to prove the robustness of the suspended ChG/silica-on-silicon slot-waveguide.

2. Problem with the mid-IR ChG-on-silicon slot-waveguide sensor

CH_4 is adopted as the target gas of the waveguide sensor, which has a fundamental absorption waveband around ~3.31 μm. Based on the high resolution transmission (HITRAN) molecule absorption database, at the wavelength near 3291 nm, the simulated absorption spectra of 50 ppm CH_4 and 2% H_2O are shown in Fig. 1(a), where the temperature T = 298 K, the pressure P = 1 atm, the light path length L = 10 cm. The influence of water vapor with a concentration level of 2% (i.e. a normal atmospheric water concentration level) is also considered. Since water vapor has a smooth absorption line in this range, the effect of water vapor can be removed by drying the injected gas sample to assure the selectivity of the sensor [1]. The absorption coefficients α_{gas} at the 3038.5 cm^{-1} absorption line is 10.715 cm^{-1} (for a pure CH_4 sample), which will be used in the characterization of the sensor.

The 3D diagram of a traditional mid-IR ChG-on-silicon slot-waveguide sensor is illustrated in Fig. 1(b), which adopts ChG materials as lower buffer and core materials. At the wavelength of 3291 nm, the refractive index of the core layer material As_2Se_3 (NBU-IR5) and the lower buffer layer material Ge-Sb-Se (NBU-IR4) are n_1 = 2.80 and n_2 = 2.42, respectively [20]. The refractive index of the target gas is n_3 = 1.0. The effective refractive index N_{eff} should satisfy the guided mode condition $n_2 < N_{eff} < n_1$. The Ge-Sb-Se buffer layer thickness is set to 2 μm. Plots of N_{eff} and PCF versus the depth-to-width ratio of the slot is shown in Fig. 1(d), where the strip width w_1 = 1 μm and slot width g = 50 nm. Guided mode condition is satisfied when the depth-to-width ratio is ≥ 40. However, a slot-waveguide with such a high depth-to-width ratio is difficult to fabricate, and in addition, the PCF is only 8.59% with this high depth-to-width ratio. Optical mode field distribution of the quasi-TE_0 mode of the ChG-on-silicon slot-waveguide is shown in Fig. 1(c), where w_1 = 1 μm, g = 50 nm and the slot height h_1 = 2 μm. Due to a low PCF and a large fabrication difficulty, ChG-on-silicon slot-waveguide is unsuitable for mid-infrared gas sensing.

3. Novel mid-IR suspended ChG/silica-on-silicon slot-waveguide sensor

3.1. Sensor structure

To solve the problem with the mid-IR ChG-on-silicon slot-waveguide sensor, a mid-IR suspended ChG/silica-on-silicon waveguide sensor is proposed and its 3D diagram is shown in Fig. 2(a). ChG is used as the core material for low waveguide loss in the mid-infrared. Silica is used as a lower support buffer layer. The silica under the waveguide core is removed for increasing light-gas interaction and decreasing waveguide loss by keeping the silica away from the core. Silica can be etched away by HF to obtain the suspended structure and a suspended width of < 10 μm can be easily realized [21], which assures the fabrication feasibility of the proposed waveguide structure.

3.2. Gas sensing theory

3.2.1. LoD and dynamic range

For the waveguide gas sensor system shown in Fig. 2(a), an HgCdTe detector (Thorlabs, PDA10JT) is used for laser beam detection, whose noise equivalent power is defined as *NEP* and bandwidth defined as *B*. The mid-infrared laser (e.g. interband cascade laser, ICL) is commercially available from Nanoplus, Germany with an output power of P_0. An electrical circuit board (ECB) is used to process the signal output from the detector and then the obtained signal is sampled by a data acquisition (DAQ) card from National Instrument.

The principle of the waveguide gas sensor is the interaction between the evanescent mode field and the target gas. The gas absorption obeys the Lambert-Beer law as [16]

$$I = I_0 \exp(-PCF\alpha_{gas}CL - \alpha_{int}L) \quad (1)$$

where I_0 is the initial intensity of the laser beam, I is the output light intensity from the waveguide, α_{gas} is the absorption coefficient of the target gas, α_{int} is the inherent loss of the waveguide including absorption loss and scattering loss, C is the gas concentration and L is the waveguide length. The absorption spectra, obtained by the ratio between I and I_0, is used for gas concentration determination. *PCF* which determines the effective optical path length, i.e. $L_{eff} = PCF \times L$, can be expressed as [18]

$$PCF = \frac{\iint_{gas} P_z \mathrm{dxdy}}{\iint_{total} P_z \mathrm{dxdy}} \quad (2)$$

where P_z is the z component of the Poynting vector along the waveguide cross-section.

Since I and I_0 correspond to the waveguide output power P and input power P_0, respectively, Eq. (1) can be transformed to

$$P = P_0 \exp(-PCF\alpha_{gas}CL - \alpha_{int}L) \quad (3)$$

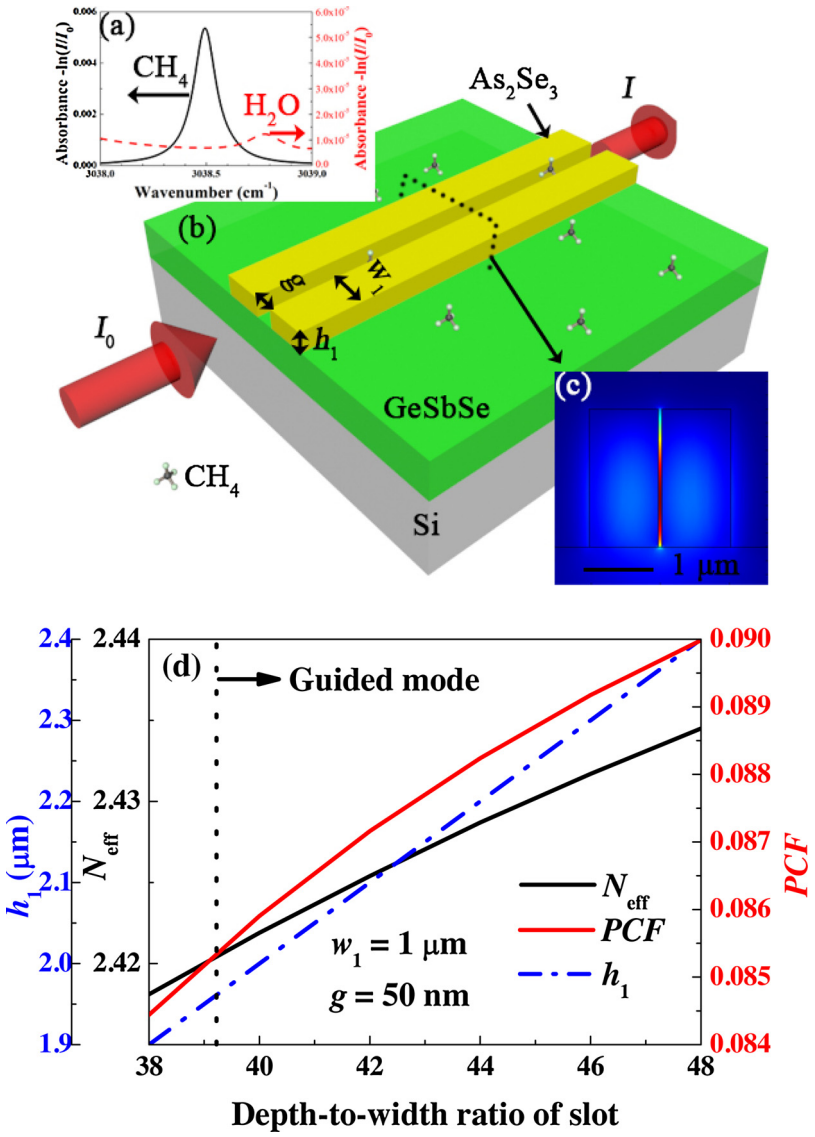

Fig. 1. (a) At $T = 298$ K, $P = 1$ atm, $L = 10$ cm, the simulated absorption spectra of CH_4 and H_2O near 3291 nm, where the CH_4 concentration is 50 ppm and H_2O is 2%. (b) 3D diagram of the ChG-on-silicon slot waveguide sensor. (c) Optical mode field distribution of the quasi-TE_0 mode of ChG-on-silicon slot waveguide, where $w_1 = 1$ μm, $g = 50$ nm and $h_1 = 2$ μm. (d) Plots of N_{eff} and PCF of the ChG-on-silicon slot waveguide versus the depth-to-width ratio of the slot, where $w_1 = 1$ μm and $g = 50$ nm.

Then the normalized absorbance can be determined by

$$\alpha = -\frac{1}{L}\ln\left(\frac{P\,|_C}{P\,|_{C=0}}\right) = -\frac{1}{L}\ln\left(\frac{\exp(-PCF\alpha_{gas}CL - \alpha_{int}L)}{\exp(-\alpha_{int}L)}\right) \quad (4)$$

The sensitivity-related factor of a waveguide sensor is the ratio between the change of light intensity due to gas absorption and the change of gas concentration, expressed as

$$S = \left|\frac{dI/I_0}{dC}\right| = PCF\alpha_{gas}L\exp(-PCF\alpha_{gas}CL - \alpha_{int}L) \quad (5)$$

With an increase of L, S increases first and then decreases, resulting in the maximum value. This is because when L is small, the change of gas concentration has a great influence on the output intensity variation; when L is large enough, waveguide loss plays a more important role than the gas absorption induced light intensity decay. The length L corresponding to the maximum value of S is defined as the optimum length of the optical waveguide L_{opt}, expressed as

$$L_{opt} = \frac{1}{PCF\alpha_{gas}C + \alpha_{int}} \quad (6)$$

At the lowest gas concentration level, i.e. the limit of detection (LoD), the output power is reduced to approximately the noise level, which is defined as the minimum power P_{min}, written as

$$P_{min} = P\,|_{C=0} - P\,|_{C=LoD} \quad (7)$$

Then the effective power signal for gas detection can be defined as

$$P_s = P_0\exp(-\alpha_{int}L) - P_0\exp(-\alpha_{int}L - PCF\alpha_{gas}LoDL) \quad (8)$$

For the detector, the power of the noise is

$$P_n = NEP\sqrt{B} \quad (9)$$

Define SNR_{min} as the minimum detectable signal-to-noise ratio of the waveguide sensor system, which is related to the detector, the ECB and the DAQ card. Then we can obtain

$$SNR_{min} = [P_0\exp(-\alpha_{int}L) - P_0\exp(-\alpha_{int}L - PCF\alpha_{gas}LoDL)]/(NEP\sqrt{B}) \quad (10)$$

Then the LoD can be obtained according to Eq. (10) as

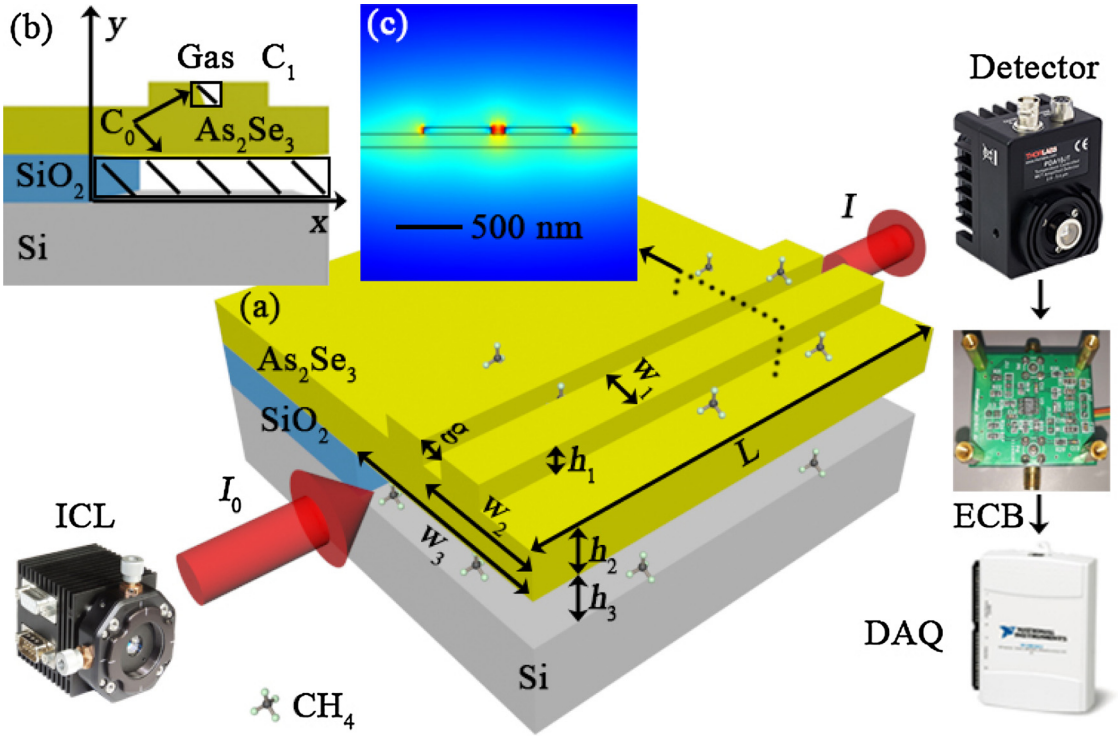

Fig. 2. (a) 3D diagram of the suspended ChG/silica-on-silicon waveguide sensor and sensor system. (b) Modelling of the waveguide for gas diffusion. (c) Optical mode field distribution of the quasi-TE_0 mode of suspended ChG/silica-on-silicon waveguide, where $w_1 = 0.5\,\mu m$, $w_2 = 3\,\mu m$, $w_3 = 6\,\mu m$, $g = 100\,nm$, $h_1 = 50\,nm$, $h_2 = 100\,nm$ and $h_3 = 2\,\mu m$.

$$LoD = \frac{-\ln\left(1 - \frac{SNR_{\min} NEP\sqrt{B}}{P_0 \exp(-\alpha_{\text{int}} L)}\right)}{PCF\alpha_{\text{gas}} L} \tag{11}$$

The normalized noise equivalent absorbance (NNEA), which indicates the background noise level of the system, can be expressed as

$$NNEA = -\frac{1}{L}\ln\left(1 - \frac{SNR_{\min} NEP\sqrt{B}}{P_0 \exp(-\alpha_{\text{int}} L)}\right) \tag{12}$$

The dynamic range of a trace gas sensor is defined as the concentration range from the LoD to the maximum concentration level (defined as $C_{\max}$) at which the sensor outputs the minimum power because of large gas absorption that can be read by the sensor system. Then we can derive

$$C_{\max} = \frac{-\ln \frac{SNR_{\min} NEP\sqrt{B}}{P_0 \exp(-\alpha_{\text{int}} L)}}{PCF\alpha_{\text{gas}} L} \tag{13}$$

Therefore the dynamic range of the sensor is defined as

$$\text{DR} = [LoD, C_{\max}] = \left[\frac{-\ln\left(1 - \frac{SNR_{\min} NEP\sqrt{B}}{P_0 \exp(-\alpha_{\text{int}} L)}\right)}{PCF\alpha_{\text{gas}} L}, \frac{-\ln \frac{SNR_{\min} NEP\sqrt{B}}{P_0 \exp(-\alpha_{\text{int}} L)}}{PCF\alpha_{\text{gas}} L}\right] \tag{14}$$

3.2.2. Response analysis

The response time of a sensor is related to the gas diffusion time from the atmosphere to the physical sensing area, mainly including the suspended area and the slot area for the proposed sensor. A modeling of the waveguide for gas diffusion analysis is shown in Fig. 2(b). The relation between gas concentration distribution and diffusion time t can be analyzed based on Fick's law. Considering static gas diffusion, the mass balance equation is shown as

$$\frac{\partial C(x, y, t)}{\partial t} + \nabla[-D\nabla C(x, y, t)] = 0 \tag{15}$$

where $C(x, y, t)$ is the concentration, and D is the binary diffusion coefficient between air and the target gas. The boundary condition can be expressed as

$$C(x, y, 0) = \begin{cases} C_0, \text{slot,suspended area} \\ C_1, \text{otherareawithgas} \end{cases} \tag{16}$$

$$C(x, y, t \to \infty) = C_1, \text{ all area with gas} \tag{17}$$

where C_0 and C_1 are the initial concentration level in the suspended/slot area and that in the atmospheric area, respectively. The average concentration in the suspended area $C_{\text{sus}}(t)$ and slot area $C_{\text{slot}}(t)$ can be determined by, respectively

$$C_{\text{slot}}(t) = \frac{\iint_{\text{slot}} C(x, y, t)\text{d}x\text{d}y}{S_{\text{slot}}} \tag{18}$$

$$C_{\text{sus}}(t) = \frac{\iint_{\text{sus}} C(x, y, t)\text{d}x\text{d}y}{S_{\text{sus}}} \tag{19}$$

where S_{slot} is the area of the slot and S_{sus} is the area of the suspended area. Then the output power $P_1(t)$ from the waveguide can be obtained by

$$P_1(t) = P_0 \exp\{-\alpha_{\text{int}} L - [PCF_{\text{slot}} C_{\text{slot}}(t) + PCF_{\text{sus}} C_{\text{sus}}(t) + PCF_{\text{other}} C_1]\alpha_{\text{gas}} L\} \tag{20}$$

where PCF_{slot}, PCF_{sus} and PCF_{other} are the PCF of the slot area, suspended area and other area, respectively. The three PCFs can be calculated using Eq. (2) by simply changing the integral area to the corresponding area.

3.3. Waveguide sensor optimization

In the following waveguide optimization, the operating wavelength of the sensor is selected as 3291 nm. The waveguide material parameters are described in Sect. 2. In order to obtain a large PCF and

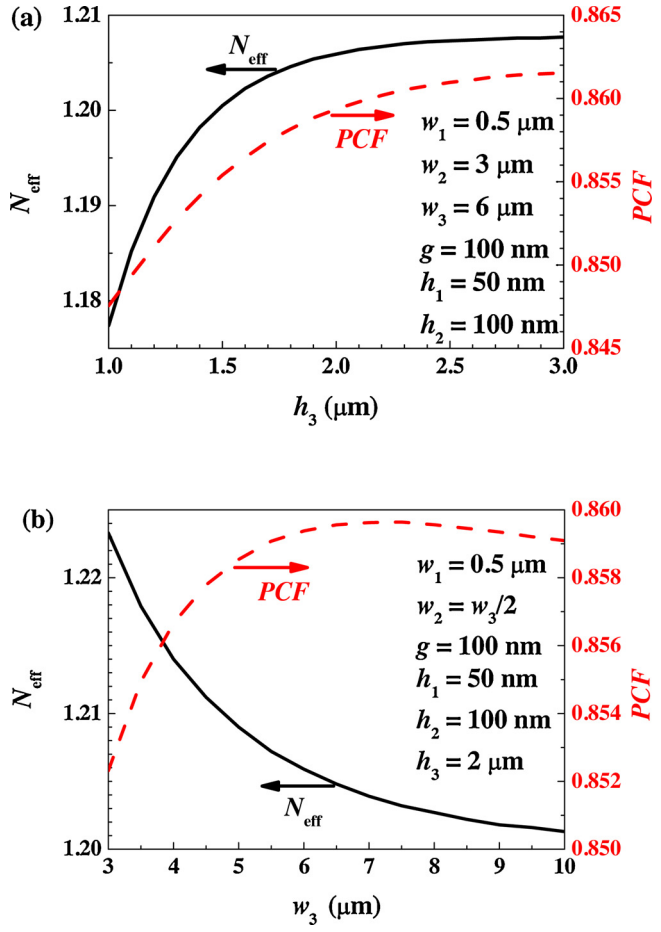

Fig. 3. (a) Plots of N_{eff} and *PCF* versus h_3, where $h_1 = 50$ nm, $h_2 = 100$ nm, $w_1 = 0.5$ μm, $w_2 = 3$ μm, $w_3 = 6$ μm, and $g = 100$ nm. (b) Plots of N_{eff} and *PCF* versus w_3, where $w_1 = 0.5$ μm, $w_2 = w_3/2$, $g = 100$ nm, $h_1 = 50$ nm, $h_2 = 100$ nm and $h_3 = 2$ μm.

satisfy guided mode condition, we use the COMSOL Multiphysics based on finite element method (FEM) to optimize the waveguide structural parameters including strip width w_1, width from the slot center to the edge w_2, suspended width w_3, slot width g, slot height h_1, slab layer thickness h_2, suspended height h_3 and waveguide length L.

3.3.1. Optimization of the suspended area parameters

The size of the suspended area influences mode field distribution and affects N_{eff} and *PCF*. Curves of N_{eff} and *PCF* versus h_3 are shown in Fig. 3(a), where $h_1 = 50$ nm, $h_2 = 100$ nm, $w_1 = 0.5$ μm, $w_2 = 3$ μm, $w_3 = 6$ μm, and $g = 100$ nm. As can be seen, with the increase of a smaller h_3, the suspended area gets larger, mode field tends to be concentrated in the core region leading to the increase of N_{eff}, and the increase of gas-light interaction area makes *PCF* to increase. N_{eff} and *PCF* gradually reach a constant value when h_3 exceeds a certain value (e.g. $h_3 = 2$ μm). So we select $h_3 = 2$ μm. Curves of N_{eff} and *PCF* versus w_3 are shown in Fig. 3(b), where $w_1 = 0.5$ μm, $w_2 = w_3/2$, $g = 100$ nm, $h_1 = 50$ nm, $h_2 = 100$ nm and $h_3 = 2$ μm. Due to a similar reason to h_3, *PCF* increases with the increase of a smaller w_3 and gradually reaches a stable value when w_3 exceeds a certain value, e.g. $w_3 = 6$ μm. Therefore we choose $w_3 = 6$ μm for maximizing the *PCF*.

3.3.2. Optimization of the slot structural parameters

Curves of *PCF* and N_{eff} versus g are shown in Fig. 4(a) and (b), respectively, where $h_1 = 50$ nm, $h_2 = 100$ nm, $h_3 = 2$ μm, $w_2 = 3$ μm, and $w_3 = 6$ μm. At a certain value of w_1, with the increase of g, mode field becomes stronger in the slot region, and the increase of light-gas interaction area makes *PCF* to increase. Note that when $g < 100$ nm, the slot-waveguide is difficult to fabricate. In order to obtain a large fabrication tolerance, we choose $w_1 = 0.5$ μm and $g = 100$ nm.

Next we optimize h_1 under the condition of $w_1 = 0.5$ μm, $w_2 = 3$ μm, $w_3 = 6$ μm, $g = 100$ nm, $h_2 = 100$ nm and $h_3 = 2$ μm. Curves of *PCF* and N_{eff} versus h_1 are shown in Fig. 4(c). With the increase of h_1, the mode field intensity over the slot region increases resulting in the decrease of N_{eff} and the increase of *PCF*. Since a slot waveguide with a low depth-to-width ratio is easy to fabricate, we choose $h_1 = 50$ nm, and the corresponding depth-to-width ratio is 0.5.

Furthermore we optimize h_2 under the condition of $w_1 = 0.5$ μm, $w_2 = 3$ μm, $w_3 = 6$ μm, $g = 100$ nm, $h_1 = 50$ nm and $h_3 = 2$ μm. Curves of *PCF* and N_{eff} versus h_2 are shown in Fig. 4(d). With the increase of h_2, mode field intensity in the slot region increases and the light-gas interaction area becomes larger, leading to the decrease of N_{eff} and the increase of *PCF*. A larger *PCF* is preferred for higher light-gas interaction, which requires a larger h_2. However, too large h_2 results in a small N_{eff}, which is against single-mode propagation. A compromise is to select $h_2 = 100$ nm.

3.3.3. Optimization of the core position

Curves of N_{eff} and *PCF* versus w_2 are shown in Fig. 4(e), where $w_1 = 0.5$ μm, $w_3 = 6$ μm, $g = 100$ nm, $h_1 = 50$ nm, $h_2 = 100$ nm and $h_3 = 2$ μm. As the core moves away from the edge, mode field will be concentrated in the core region, making the increase of N_{eff} and the decrease of *PCF*. *PCF* gradually reaches a stable value when $w_2 = 3$ μm. So we select $w_2 = 3$ μm, which results in a PCF of 85.77% and an effective refractive index of $N_{eff} = 1.2009$.

3.3.4. Optimization of the sensor waveguide length

Based on Eq. 5, the sensitivity-related factor S correlates to waveguide length L and propagation loss α_{int}. A typical fabricated ChG waveguide loss is about 0.5–2.6 dB/cm [22–24]. Without loss of generality, we set $\alpha_{int} = 3$ dB/cm. Curve of S versus L is shown in Fig. 4(f). The inflection point corresponding to the maximum value of S and the optimal waveguide length L_{opt}, which are determined to be $L_{opt} = 1.45$ cm and $S = 4.89$.

3.3.5. Summary of the optimization

The final optimized waveguide parameters are listed in Table 1. With the optimal waveguide structure, optical mode field distribution of the quasi-TE_0 mode of suspended ChG/silica-on-silicon waveguide is shown in the inset of Fig. 2(c). Most of the light is found to be confined in the slot area and the core surrounding area, which provides the basis for the interaction between gas and light.

4. Waveguide sensor characteristics

In this section, we will discuss the sensing characteristics of the optimum suspended ChG slot-waveguide sensor proposed in Sect. 3 by numerical simulation. Typically, a HgCdTe detector (Thorlabs, PDA10JT) is used for laser beam detection with an operating wavelength range of 2.0–5.4 μm, a NEP of 2.08×10^{-11} $WHz^{-1/2}$ and a bandwidth (B) of 160 kHz. The output power P_0 from the mid-infrared laser (e.g. interband cascade laser, ICL) is set to be $P_0 = 10$ mW, which is an acceptable output power of an ICL commercially available from Nanoplus, Germany.

4.1. Sensor response curve versus CH_4 concentration

By strictly controlling the temperature of the laser, the relative fluctuation of the laser power can be less than ± 0.2% [25]. The waveguide output power without gas absorption versus time is shown in Fig. 5(a), where $L = 1.45$ cm, $\alpha_{int} = 3.0$ dB/cm and $(1–0.2\%) \times 10$ mW $\leq |P_0| \leq (1 + 0.2\%) \times 10$ mW. The noise power P_n of the detector and the minimum detectable noise power $SNR_{min}P_n$ of

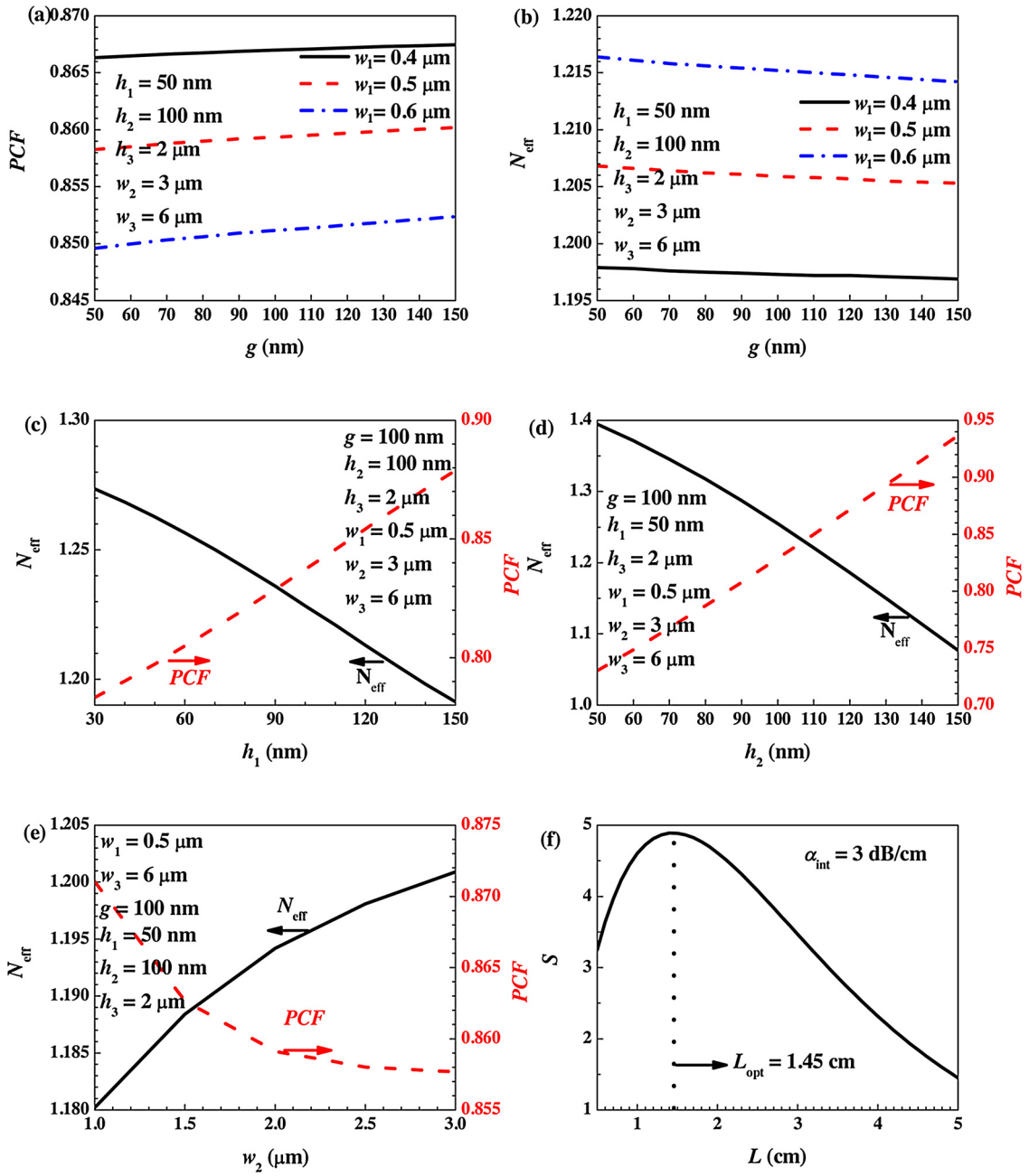

Fig. 4. (a) Plots of *PCF* versus *g*, where h_1 = 50 nm, h_2 = 100 nm, h_3 = 2 μm, w_2 = 3 μm, w_3 = 6 μm, and w_1 = 0.4 μm, 0.5 μm and 0.6 μm. (b) Plots of N_{eff} versus *g*, where h_1 = 50 nm, h_2 = 100 nm, h_3 = 2 μm, w_2 = 3 μm, w_3 = 6 μm, and w_1 = 0.4 μm, 0.5 μm and 0.6 μm. (c) Plots of N_{eff} and *PCF* versus h_1, where w_1 = 0.5 μm, w_2 = 3 μm, w_3 = 6 μm, *g* = 100 nm, h_2 = 100 nm and h_3 = 2 μm. (d) Plots of N_{eff} and *PCF* versus h_2, where w_1 = 0.5 μm, w_2 = 3 μm, w_3 = 6 μm, *g* = 100 nm, h_1 = 50 nm and h_3 = 2 μm. (e) Plots of N_{eff} and *PCF* versus w_2, where w_1 = 0.5 μm, w_3 = 6 μm, *g* = 100 nm, h_1 = 50 nm, h_2 = 100 nm and h_3 = 2 μm. (f) Plot of *S* versus *L*, where α_{int} = 3 dB/cm.

the sensor system versus time are shown in Fig. 5(b). Only considering the fluctuation of laser power, curves of waveguide output power and the normalized absorbance versus CH_4 concentration are shown in Fig. 5(c), where the waveguide parameters are taken as those listed in Table 1. The error bar shows the influence of the power instability. It can be found that within a wide concentration range, the output power from the waveguide decreases nonlinearly with the concentration which obeys the Lambert-Beer law shown by Eq. (3).

4.2. LoD and detection range

Based on Eqs. (11–13), curves of *LoD*, NNEA and C_{max} versus SNR_{min} are shown in Fig. 6. The increase of SNR_{min} makes the noise level of the system higher at the same signal level, resulting in the decrease of the sensor sensitivity. Therefore, *LoD* becomes larger and C_{max} becomes smaller with the increase of SNR_{min} at the optimal waveguide length of 1.45 cm. High SNR_{min} means large minimum detectable power, which increases NNEA. With an easily-realizable SNR_{min} of 10, the *LoD* is 1.70 ppm, the minimum detectable power is $10NEP\sqrt{B} = 8.32 \times 10^{-8}$ W, the NNEA is 1.56×10^{-5} cm^{-1}, and the detection range is [1.70 ppm, 80.26%].

4.3. Response time

The response time of the sensor is determined by the gas diffusion time. When the sensor is placed in a new gas environment, under the

Table 1
Optimized parameters for the suspended ChG/silica-on-silicon slot-waveguide sensor.

Waveguide parameters	Value
Wavelength, λ	3291 nm
Strip width, w_1	0.5 μm
Width from the slot center to the edge, w_2	3 μm
Suspended width, w_3	6 μm
Slot width, g	100 nm
Slot height, h_1	50 nm
Slab layer thickness, h_2	100 nm
Suspended height, h_3	2 μm
Waveguide length, L	1.45 cm (@3dB/cm loss)
Performance	Value
Mode effective index, N_{eff}	1.2009
PCF	85.77%

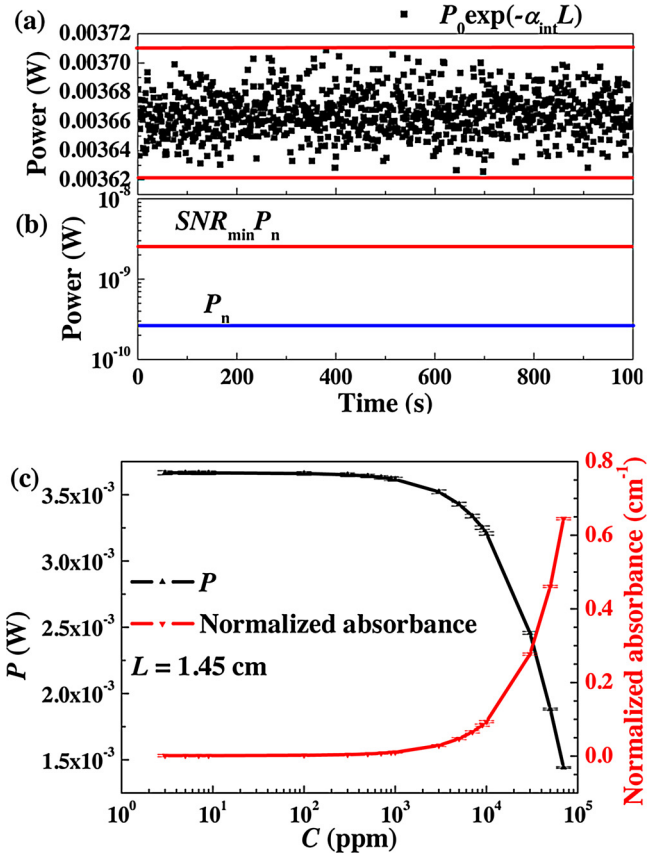

Fig. 5. (a) Plot of waveguide output power without gas absorption versus time when the fluctuation of laser power is 0.2%. (b) Plot of the noise power of the detector and the minimum detectable noise power of the sensor system versus time. (c) Plots of waveguide output power and normalized absorbance versus CH_4 concentration, where the waveguide parameters are taken as those listed in Table 1.

condition of static free diffusion, only the gas diffusion process in the suspended area and the slot area are considered. When the initial CH_4 concentration level in the atmosphere is $C_1 = 5000$ ppm and that in the slot and suspended area are $C_0 = 0$, curve of $P_1(t)$ versus diffusion time t is shown in Fig. 7(a), where the gas diffusion starts at $t = 0$ and the gas diffusion coefficient of CH_4 is 0.208 cm^2/s [11]. The 90-10% fall time is determined to be 2.3 μs. When the initial CH_4 concentration level in the slot and suspended area is $C_0 = 5000$ ppm and that in the atmosphere is $C_1 = 0$, curve of $P_1(t)$ versus t is shown in Fig. 7(b). At this time, the 10–90% rise time is calculated to be 2.4 μs. Because the slot area and the suspended area of the waveguide are exposed to the atmosphere,

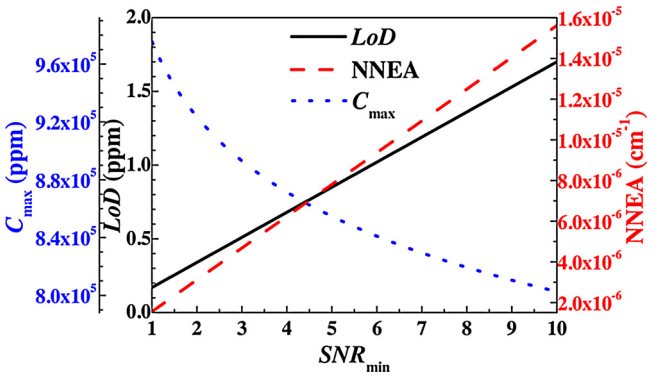

Fig. 6. Curves of *LoD*, NNEA and C_{max} versus SNR_{min} of the optimal waveguide sensor, where $L = 1.45$ cm, $\alpha_{int} = 3.0$ dB/cm, and $P_0 = 10$ mW.

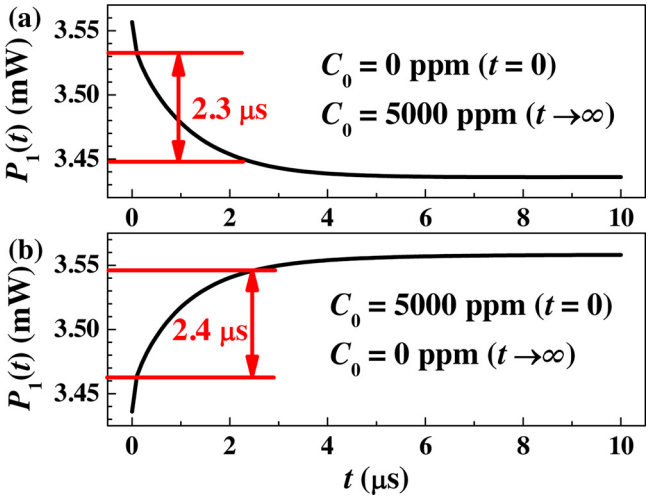

Fig. 7. Plots of the output power $P_1(t)$ versus t, where (a) the initial concentration levels at $t = 0$ in the slot /suspended areas and the atmosphere are 0 and 5000 ppm, respectively, and (b) the initial concentration levels at $t = 0$ in the slot /suspended areas and the atmosphere are 5000 and 0 ppm, respectively. The waveguide parameters are taken as those listed in Table 1.

the diffusion distance is as short as the level of μm, which leads to a fast response to the level of μs. Since the gas diffusion of a fiber sensor is usually realized through the two ends, the response time is longer than 1 s for the 1cm-long photonic crystal fiber sensor [26].

4.4. Influences of ambient temperature and pressure change

Ambient temperature change will modify the refractive index of the core and influence the sensing characteristics. With a thermo-optic coefficient of $\sim 4 \times 10^{-5}$ for the core material of As_2Se_3, the influence of ambient temperature change on the sensor is shown in Fig. 8(a). Within the range of −30 to 60 °C, as the temperature increases, *PCF* decreases and *LoD* increases. But the variation of *PCF* is < 0.0004 and the variation of *LoD* is < 1 ppm. Hence the change of ambient temperature shows almost no influence on the sensing performance because of low thermo-optic coefficient of the waveguide core material.

Ambient pressure change will influence the absorption coefficient α_{gas} and thus affect the sensing characteristics. The influence of ambient pressure change on the sensor is shown in Fig. 8(b). Within the range of 0.5–1.5 at m, as the pressure increases, α_{gas} increases leading to the decrease of *LoD*. The variation of *LoD* is < 0.04 ppm. Hence the change of ambient pressure shows almost no influence on the sensing performance because of a small change of α_{gas}.

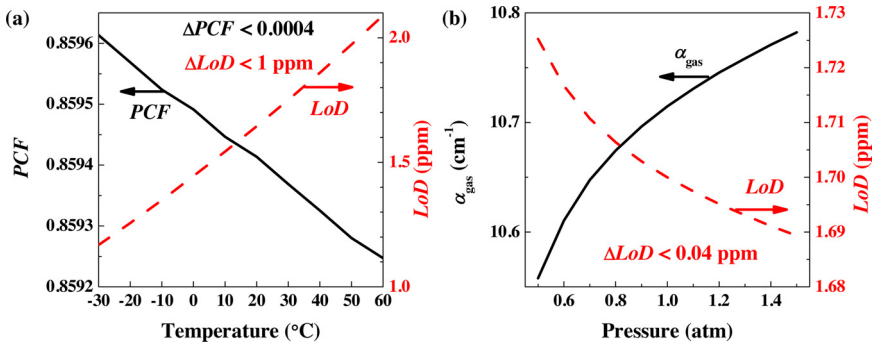

Fig. 8. (a) Plots of *PCF* and *LoD* versus the ambient temperature, where the waveguide parameters are taken as those listed in Table 1, and $P = 1$ atm. (b) Plots of α_{gas} and *LoD* versus the ambient pressure, where the waveguide parameters are taken as those listed in Table 1, and $T = 25$ °C.

4.5. Influence of the photo-thermal effect

Light absorption by gas will generate heat and change the temperature of both gas and waveguide, which is named photo-thermal effect [27]. However, the change of temperature in the silica waveguide at an incident power of 40 mW and a CH_4 concentration level of 10^4 ppm is less than 1 °C. Based on the analysis in Sect. 4.4, a large ambient temperature change of −30 to 60 °C has almost no effect on the suspended waveguide sensor. So the influence of the photo-thermal effect on the effective refractive index and *LoD* can be ignored.

4.6. Fabrication tolerance

4.6.1. Fabrication error of waveguide

Considering the accuracy of the available mature fabrication technologies, h_1 (@50 nm) with a fabrication error of ± 20 nm, h_2 (@100 nm) and g (@100 nm) with a fabrication error of ± 50 nm, w_1 (@500 nm) with a fabrication error of ± 100 nm, h_3 (@2 μm) with a fabrication error of ± 0.5 μm, and w_2 (@3 μm) and w_3 (@6 μm) with a fabrication error of ± 1 μm can be easily realized. Plots of the variation of *PCF* (Δ*PCF*), *LoD* (Δ*LoD*) and N_{eff} (ΔN_{eff}) versus the fabrication errors of h_1, h_2, g, w_1, h_3, w_2, and w_3 are shown in Fig. 9(a)–(g), respectively. With the fabrication errors of h_1, g, w_1, h_3, w_2, and w_3, the suspended waveguide is still in single mode and the relative change of Δ*PCF* and Δ*LoD* is < 2%. The fabrication error of h_2 influences much on Δ*PCF* and Δ*LoD* with a relative change of < 20%. Considering these fabrication tolerances, w_1, w_2 and g can be achieved by electron beam lithography and etching, h_1 and h_2 can be guaranteed by magnetron sputtering or thermal evaporation and etching, w_3 can be achieved by HF etching, and h_3 can be achieved by chemical vapor deposition, as depicted in Table 2.

The fabrication process of the suspended ChG/silica-on-silicon slot-waveguide is as follows. First, SiO_2 layer is fabricated by chemical vapor deposition on the silicon substrate. Then the ChG film is deposited on SiO_2 by thermal evaporation. The slot structure can be obtained by electron beam lithography and inductively coupled plasma (ICP) etching. This is one challenge in the fabrication process. It is necessary to strictly control the etching time and other parameters to achieve a slot structure with vertical sidewall and accurate thickness. Finally, the suspended structure can be obtained by HF etching. This is another challenge in the fabrication process. If the suspended structure is too wide, the upper ChG layer may collapse. The width of the suspended structure can be guaranteed by controlling the HF concentration level and reaction time.

4.6.2. Refractive index error resulting from fabrication

Thermal evaporation is a commonly used method for preparing ChG films with a fast evaporation speed, large area and low cost. However, the refractive index of ChG film may be changed because the compositions of ChG glass may be altered at different temperatures, and the error of the refractive index is generally less than 0.2 through a standard mature process [28]. A refractive index error within −0.2–0.2 of n_1 (2.8) on Δ*PCF*, Δ*LoD* and ΔN_{eff} are considered, as shown in Fig. 10. The obtained relative error of Δ*PCF* and Δ*LoD* is less than 3% and the suspended ChG/silica-on-silicon slot-waveguide is still in guided mode. This indicates that it is unnecessary to pay more attention to the refractive index error resulting from film deposition.

4.6.3. Waveguide loss tolerance

Waveguide loss is assumed to be 3.0 dB/cm in the evaluation of the sensor performance, which is a typical loss for ChG waveguide. However, the waveguide structure proposed in the study is not the same

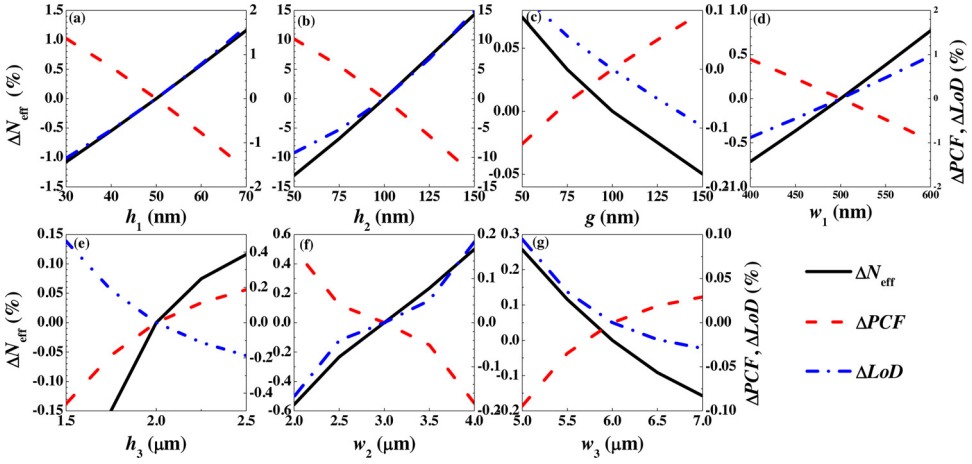

Fig. 9. Plots of Δ*PCF*, Δ*LoD* and ΔN_{eff} versus the fabrication errors of (a) h_1, (b) h_2, (c) g, (d) w_1, (e) h_3, (f) w_2, and (g) w_3.

Table 2
The allowed range of fabrication error and feasibility of the waveguide sensor.

Parameter	Technique	Target value	Allowed range	Feasibility
w_1	Electron beam lithography and etching	500 nm	± 100 nm	Feasible
w_2	Electron beam lithography and etching	3 μm	± 1 μm	Feasible
w_3	HF etching	6 μm	± 1 μm	Feasible
g	Electron beam lithography and etching	100 nm	± 50 nm	Feasible
h_1	Thermal evaporation and etching	50 nm	± 20 nm	Feasible
h_2	Thermal evaporation and etching	100 nm	± 100 nm	Feasible
h_3	Chemical vapor deposition	2 μm	± 0.5 μm	Feasible
n_1	Thermal evaporation	2.8	± 0.2	Feasible

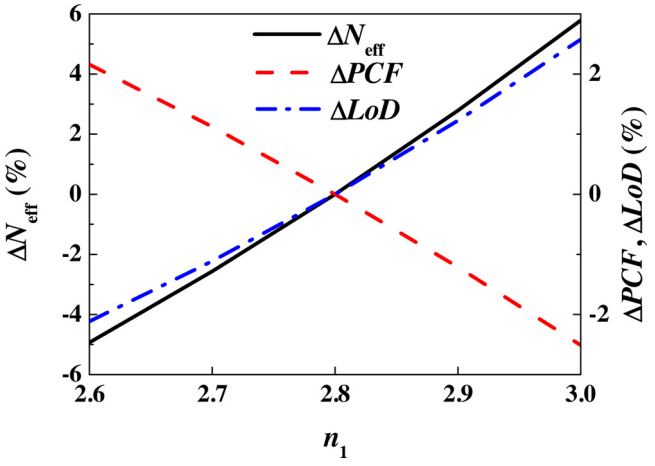

Fig. 10. Plots of ΔPCF, ΔLoD and ΔN_{eff} versus the fabrication error of n_1.

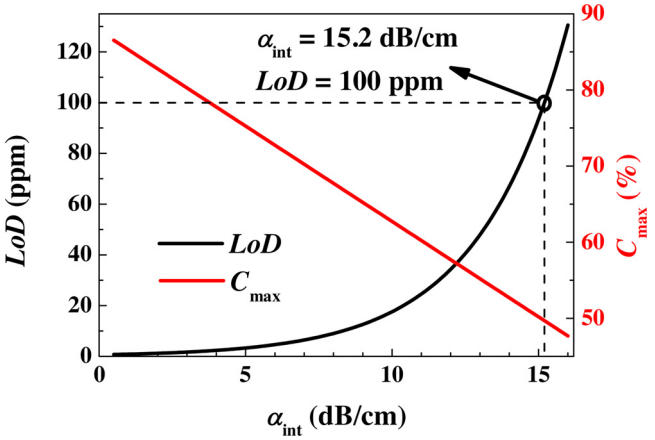

Fig. 11. Curves of LoD and C_{max} versus α_{int}, where the waveguide parameters are taken as those listed in Table 1.

as the traditional ChG waveguide. Under a waveguide loss from 0.5 dB/cm to 15 dB/cm, the relation between LoD, C_{max} and the waveguide loss is shown in Fig. 11. Based on Eqs. (8) and (11), the increased loss declines the output power from the waveguide P_s, so LoD increases under the same minimum detectable noise power level and SNR_{min}. Based on Eqs. (13) and (14), the declined output power decreases C_{max} and shortens the detection range of the sensor system. For some typical applications, e.g. the CH_4 detection in coal mining environment, the LoD needs to be < 100 ppm, and the waveguide loss needs to be < 15 dB/cm. For obtaining a low LoD (e.g. < 10 ppm), a small waveguide loss (e.g. < 8 dB/cm) is required.

4.7. Comparison and discussion

There are some other reported ChG or Si waveguide sensors using evanescent field for gas sensing, which are compared with the performances of the reported sensor as shown in Table 3. Several methods including the finite difference method (FDM), finite-difference time-domain (FDTD) and finite element method (FEM) are used for the calculation of the PCF. Experimental results show that a more accurate PCF can be obtained by FEM [18,29]. Hence FEM was used to calculate the PCF of the waveguide structures reported in [11,15–17], and the results are shown at the right hand column in Table 3. It can be seen that, the PCF calculated by FDM and FDTD are larger than that by FEM. Although the waveguide sensor reported in [11] has a large PCF, the sensor is based on silicon material on CaF_2 substrate, whose operating wavelength cannot be extended to that of the ChG material platform; in addition, since SiO_2 is used as the support layer in the input port and output port of the waveguide, the sensor has great loss in the mid-infrared. Compared to other waveguide sensors, our proposed suspended ChG/silica-on-silicon slot-waveguide has the largest PCF, which is 10 times higher than other ChG rectangular waveguide sensors. This means that the effective path length can be increased by at least 10 times and the LoD can be reduced by at least 10 times. Therefore the suspended ChG/silica-on-silicon slot-waveguide sensor is of great significance for device miniaturization and for the improvement of the sensing performance in the mid-infrared.

Recently, some works used hollow-core fiber or the micro-structured fibers to enhance the absorption length [26,30,31]. Compared with the fiber-type gas sensors, an obvious advantage of the waveguide sensor is that the sensing operation can be implemented on a single chip, provided that the sensing module, the laser and the detection are fabricated on a single chip. The sensor chip has a high laser coupling efficiency between the laser/detector and the sensing unit, and is immune to temperature change and vibration. Furthermore, the reported fiber-type gas sensor has a long response time due to the slow gas

Table 3
Comparison among the proposed suspended ChG/silica-on-silicon sensor and other reported waveguide sensors.

Refs.	Waveguide material	Waveguide type	λ (μm)	Reported PCF	Reported method	PCF (FEM[a])
[16]	ChG	Rectangular	1.55	5%	FDM	4.61%
[15]	ChG	Rectangular	7.70	5%	FDTD	1.75%
[17]	ChG	Rectangular	4.30	8%	FDTD	3.67%
[11]	Si	Rib slot	4.47	68.0%	FDTD	67.00%
This paper	ChG	Suspended slot	3.291	85.77%	FEM	85.77%

[a] These results were calculated using FEM on the reported waveguide structures.

diffusion through the hollow core [26,30] or drilled holes by laser processing [31]. However, the proposed waveguide sensor adopts air as cladding material and the sensing area is directly exposed to the atmosphere, which speeds up the sensor response to the level of μs.

5. Conclusions

A novel suspended ChG/silica-on-silicon slot-waveguide sensor was proposed for mid-IR absorption spectroscopic gas sensing. The waveguide parameters were optimized for single-mode propagation, PCF enhancement and reasonable fabrication process. The demonstrated PCF is 85.77% at the wavelength of 3291 nm, which is at least 10 times higher than other reported ChG rectangular waveguides. CH_4 was adopted as the target gas for performance evaluation of the suspended ChG/silica-on-silicon slot-waveguide sensor. An optimal waveguide length of 1.45 cm was determined with a typical waveguide loss of 3 dB/cm. The LoD of CH_4 was 1.70 ppm under a minimum detectable SNR of 10 of the data processing module. Ambient temperature/pressure and fabrication errors were found to have less effect on the sensor performance. Future work will focus on the fabrication of a suspended ChG/silica-on-silicon slot-waveguide sensor as well as carrying out gas measurements for performance evaluation of such waveguide sensors.

Acknowledgements

The authors wish to express their gratitude to the National Natural Science Foundation of China (Nos. 61775079, 61604151, 61627823), Key Science and Technology R&D program of Jilin Province, China (Nos. 20180201046GX, 20190101016JH), Industrial Innovation Program of Jilin Province, China (No. 2017C027), and the US National Science Foundation (NSF) ERC MIRTHE award and Robert Welch Foundation (No. C-0586).

References

[1] C.T. Zheng, W.L. Ye, N.P. Sanchez, C.G. Li, L. Dong, Y.D. Wang, R.J. Griffin, F.K. Tittel, Development and field deployment of a mid-infrared methane sensor without pressure control using interband cascade laser absorption spectroscopy, Sens. Actuators B: Chem. 244 (2017) 365–372.
[2] B. Li, C.T. Zheng, H.F. Liu, Q.X. He, W.L. Ye, Y. Zhang, J.Q. Pan, Y.D. Wang, Development and measurement of a near-infrared CH_4 detection system using 1.654 μm wavelength-modulated diode laser and open reflective gas sensing probe, Sens. Actuators B: Chem. 225 (2016) 188–198.
[3] F. Song, C.T. Zheng, W.H. Yan, W.L. Ye, Y.D. Wang, F.K. Tittel, Interband cascade laser based mid-infrared methane sensor system using a novel electrical-domain self-adaptive direct laser absorption spectroscopy (SA-DLAS), Opt. Express 25 (2017) 31876–31888.
[4] M. Dong, C.T. Zheng, D. Yao, G.Q. Zhong, S.Z. Miao, W.L. Ye, Y.D. Wang, F.K. Tittel, Double-range near-infrared acetylene detection using a dual spot-ring Herriott cell (DSR-HC), Opt. Express 26 (2018) 12081–12091.
[5] Q.X. He, C.T. Zheng, M.H. Lou, W.L. Ye, Y.D. Wang, F.K. Tittel, Dual-feedback mid-infrared cavity-enhanced absorption spectroscopy for H_2CO detection using a radio-frequency electrically-modulated interband cascade laser, Opt. Express 26 (2018) 15436–15444.
[6] Q.Y. Du, Z.Q. Luo, H.K. Zhong, Y.F. Zhang, Y.Z. Huang, T.J. Du, W. Zhang, T. Gu, J.J. Hu, Chip-scale broadband spectroscopic chemical sensing using an integrated supercontinuum source in a chalcogenide glass waveguide, Photonics Res. 6 (2018) 506–510.
[7] L.F. Gao, X. Yang, Y. Shu, X.W. Chen, J.H. Wang, Ionic liquid-based slab optical waveguide sensor for the detection of ammonia in human breath, J. Colloid Interface Sci. 512 (2018) 819–825.
[8] C. Kraeh, J.L. Martinez-Hurtado, A. Popescu, H. Hedler, J.J. Finley, Slow light enhanced gas sensing in photonic crystals, Opt. Mater. 76 (2018) 106–110.
[9] G.Q. Wang, C.N. Wang, S.Q. Sun, An optical waveguide sensor based on mesoporous silica films with a comparison to surface plasmon resonance sensors, Sens. Actuators B: Chem. 255 (2018) 3400–3408.
[10] D.H. Niu, X.B. Wang, S.Q. Sun, M.H. Jiang, Q. Xu, F. Wang, Y.D. Wu, D.M. Zhang, Polymer/silica hybrid waveguide temperature sensor based on asymmetric Mach-Zehnder interferometer, J. Optics-UK 20 (2018) 045803.
[11] B. Kumari, R.K. Varshney, B.P. Pal, Design of chip scale silicon rib slot waveguide for sub-ppm detection of N_2O gas at mid-IR band, Sens. Actuators B: Chem. 255 (2018) 3409–3416.
[12] E. Esveld, J. Bows, M. Vollebregt, R.V.D. Sman, In-situ single mode dielectric measurements of microwaveable snack pellets, J. Food Eng. 231 (2018) 109–122.
[13] E. Farkas, A. Szekacs, B. Kovacs, M. Olah, R. Horvath, I. Szekacs, Label-free optical biosensor for real-time monitoring the cytotoxicity of xenobiotics: a proof of principle study on glyphosate, J. Hazard. Mater. 351 (2018) 80–89.
[14] T. Hu, B.W. Dong, X.S. Luo, T.Y. Liow, J.F. Song, C. Lee, G.Q. Lo, Silicon photonic platforms for mid-infrared applications [Invited], Photonics Res. 5 (2017) 417–430.
[15] A. Gutierrez-Arroyo, E. Baudet, L. Bodiou, J. Lemaitre, I. Hardy, F. Faijan, B. Bureau, V. Nazabal, J. Charrier, Optical characterization at 7.7 μm of an integrated platform based on chalcogenide waveguides for sensing applications in the mid-infrared, Opt. Express 24 (2016) 23109–23117.
[16] J. Charrier, M.L. Brandily, H. Lhermite, K. Michel, B. Bureau, F. Verger, V. Nazabal, Evanescent wave optical micro-sensor based on chalcogenide glass, Sens. Actuators B: Chem. 173 (2012) 468–476.
[17] A. Gutierrez-Arroyo, E. Baudet, L. Bodiou, V. Nazabal, E. Rinnert, K. Michel, B. Bureau, F. Colas, J. Charrier, Theoretical study of an evanescent optical integrated sensor for multipurpose detection of gases and liquids in the Mid-Infrared, Sens. Actuators B: Chem. 242 (2017) 842–848.
[18] L. Tombez, E.J. Zhang, J.S. Orcutt, S. Kamlapurkar, W.M.J. Green, Methane absorption spectroscopy on a silicon photonic chip, Optica 4 (2017) 1322–1325.
[19] Z. Han, P. Lin, V. Singh, L. Kimerling, J. Hu, K. Richardson, A. Agarwal, D.T.H. Tan, On-chip mid-infrared gas detection using chalcogenide glass waveguide, Appl. Phys. Lett. 108 (2016) 141106.
[20] http://www.ir-glass.com/usr/uploads/2018/02/1392963412.pdf.
[21] D. Kita, H. Lin, J. Li, Z. Han, P. Su, T. Gu, A. Agarwal, A. Yadav, K. Richardson, J. Hu, Suspended chalcogenide microcavities for ultra-sensitive chemical detection, IEEE Sens. (2016).
[22] X. Gai, S. Madden, D.Y. Choi, D. Bulla, B. Luther-Davies, Dispersion engineered $Ge_{11.5}As_{24}Se_{64.5}$ nanowires with a nonlinear parameter of $136W^{-1}m^{-1}$ at 1550nm, Opt. Express 18 (2010) 18866–18874.
[23] J.F. Viens, C. Meneghini, A. Villeneuve, T.V. Galstian, E.J. Knystautas, M.A. Duguay, K.A. Richardson, T. Cardinal, Fabrication and characterization of integrated optical waveguides in sulfide chalcogenide glasses, J. Lightwave Technol. 17 (1999) 1184–1191.
[24] X. Gai, D.Y. Choi, S. Madden, B. Luther-Davies, Polarization-independent chalcogenide glass nanowires with anomalous dispersion for all-optical processing, Opt. Express 20 (2012) 13513–13521.
[25] P. Su, Z. Han, D. Kita, P. Becla, H. Lin, S. Deckoff-Jones, K. Richardson, L.C. Kimerling, J. Hu, A. Agarwal, Monolithic on-chip mid-IR methane gas sensor with waveguide-integrated detector, Appl. Phys. Lett. 114 (2019) 051103.
[26] Y.L. Hoo, W. Jin, C. Shi, H.L. Ho, D.N. Wang, S.C. Ruan, Design and modeling of a photonic crystal fiber gas sensor, Appl. Opt. 42 (2003) 3509–3515.
[27] Y. Qi, F. Yang, Y. Lin, W. Jin, H.L. Ho, Nanowaveguide enhanced photothermal interferometry spectroscopy, J. Lightwave Technol. 35 (2017) 5267–5275.
[28] D.A.P. Bulla, R.P. Wang, A. Prasad, A.V. Rode, S.J. Madden, B. Luther-Davies, On the properties and stability of thermally evaporated Ge–As–Se thin films, Appl. Phys. A-Mater. 96 (2009) 615–625.
[29] C. Ranacher, C. Consani, A. Tortschanoff, R. Jannesari, M. Bergmeister, T. Grille, B. Jakoby, Mid-infrared absorption gas sensing using a silicon strip waveguide, Sens. Actuator A: Phys. 277 (2018) 117–123.
[30] L.E. Hu, C.T. Zheng, D. Yao, D. Yu, Z.W. Liu, J. Zheng, Y.D. Wang, F.K. Tittel, A hollow-core photonic band-gap fiber based methane sensor system capable of reduced mode interference noise, Infrared Phys. Technol. 97 (2019) 101–107.
[31] H. Lehmann, H. Bartelt, R. Willsch, R. Amézcua-Correa, J.C. Knight, In-line gas sensor based on a photonic bandgap fiber with laser-drilled lateral microchannels, IEEE Sens. J. 11 (2011) 2926–2931.

Mingquan Pi received his BS degree from the College of Electronic Science and Engineering, Jilin University, PR China, in 2018. He entered the master course in the same year. Now he majors in Circuits and Systems, and his research interests include waveguide gas sensor and optical waveguide device.

Chuantao Zheng received his MS degree and Ph.D degree in 2007 and 2010, respectively, from the College of Electronic Science and Engineering, Jilin University, PR China. Currently he is a professor at Jilin University, PR China. His research interests include optoelectronic devices and their applications in sensing and optical communications. Dr. Zheng has published more than 150 scientific journal articles in the above technical fields as a first author or corresponding author.

Ran Bi received her BS degree from the College of Electronic Science and Engineering, Jilin University, PR China, in 2018. She entered the master course in the same year. Now she majors in Circuits and Systems, and her research interests include transparent conductive oxide films in the infrared and their applications.

Huan Zhao received his BS degree from the College of Electronic Science and Engineering, Jilin University, PR China, in 2017. He entered the master course in the same year. Now he majors in Integrated Circuit and Engineering, and his research interests include hybrid integrated laser and optical waveguide device.

Lei Liang received his Ph.D degree from the College of Electronic Science and Engineering, Jilin University, PR China, in 2014. Currently he is an assistant researcher in State Key Laboratory of Luminescence and Applications, Changchun Institute of Optics Fine Mechanics and Physics, Chinese Academy of Sciences. His research interests include optical waveguide device, semiconductor laser, and SOA.

Yu Zhang received his MS degree and Ph.D degree in 2007 and 2010, respectively, from College of Electronic Science and Engineering, Jilin University, PR China. Now he is a

professor in the same college. His research interests include quantum dot materials, LEDs and solar cells.

Yiding Wang received his MS degree in Physics in 1991 from Jilin University. Now he is a professor in State Key Laboratory on Integrated Optoelectronics, College of Electronic Science and Engineering, Jilin University, P.R. China. He is active in the fields of gas sensors using infrared techniques and the fabrication of mid-infrared LEDs and LDs.

Frank K. Tittel received his B.S. degree in 1955 and the Ph.D degree in 1959 from Oxford University. Now he is the J. S. Abercrombie Professor in the School of Engineering, Rice University, Houston, TX. Professor Frank Tittel has been involved in many innovative developments in quantum electronics and laser technology since the discovery of the laser in 1960, with applications ranging from laser spectroscopy to environmental monitoring. The most recent designs utilize novel quantum cascade and interband cascade lasers to achieve compact, robust instrumentation that can be deployed for field applications, such as at NASA's Johnson Space Center related to air and water quality issues relevant to the International Space Station, for urban formaldehyde monitoring funded by the Environmental Protection Agency, as well as the National Institute of Health, for non-invasive NO and CO detection in biomedical systems and the National Science Foundation (http://lasersci.rice.edu/).